Shifting the Paradigm: A Functional Hole-Selective Transport Layer for Chalcopyrite Solar Cells

Taowen Wang, Longfei Song, Sevan Gharabeiki, Mohit Sood, Aubin JC.M. Prot, Ricardo G. Poeira, Michele Melchiorre, Nathalie Valle, Adrian-Marie Philippe, Sebastjan Glinsek, Emmanuel Defay, Phillip J. Dale, and Susanne Siebentritt*

High-efficiency $Cu(In,Ga)Se_2$ solar cells rely on Ga grading to mitigate back surface recombination. However, the inhomogeneous absorber has drawbacks, including increased non-radiative loss and inadequate absorption. Therefore, literatures demand a paradigm shift of using a hole-transport layer to passivate the back surface. Herein, a functional hole-transport layer is demonstrated as an alternative to Ga grading. The novel hole-transport layer is prepared as a double-layer: co-evaporated $CuGaSe_2$ covered by solution combustion synthesis prepared In_2O_3. As demonstrated by micrographs, elemental mapping, and photoluminescence spectroscopy, the oxide layer improves thermal stability and prevents Ga diffusion. However, during the absorber deposition, a complete ion exchange of In and Ga converts $CuGaSe_2/In_2O_3$ into $CuInSe_2/GaO_x$. Incorporating this hole-transport layer in co-evaporated nongraded $CuInSe_2$ solar cells leads to significantly increased minority carrier lifetime from 5 to 113 ns, yielding an 80 meV improvement in quasi-Fermi-level splitting. The devices exhibit improved open-circuit voltage, as well as a promising fill factor of over 71%, indicating good hole-transport properties. In these results, the passivation effect and good hole-transport properties of the hole-transport layer are experimentally demonstrated. Thus, high-efficiency solar cells can be achieved by using a functional hole-transport layer without relying on Ga grading.

1. Introduction

Chalcopyrite-based thin-film solar cells are industrially produced[1–3] and have achieved stable efficiencies exceeding 23%.[4,5] Remarkably, these high efficiencies employ a full-area metal back contact[4–6] with high recombination velocity ranging from 10^5 to 10^7 $cm\,s^{-1}$.[7] To mitigate backside recombination, record solar cells incorporate a gradient of the Ga content that increases the energy of the conduction band minimum toward the back contact.[4–6,8–10] We have recently demonstrated that this gradient reduces back contact recombination, and thus the non-radiative loss in open-circuit voltage (V_{oc}), by about 50 mV.[11] While this gradient can reduce backside recombination by keeping minority carrier away from the back contact,[9] it also introduces various losses: 1) the thin zone of the minimum bandgap (notch position) leads to non-absorption losses in short-circuit current density (J_{sc}),[12] 2) gradual absorption onset could cause radiative losses in V_{oc},[13,14] and 3) high Ga region near the back contact exhibits extremely low carrier lifetimes (100 ps)[15] due to additional deep defects.[16,17] Moreover, it requires an unnecessarily thick absorber to build the required Ga gradient, increasing production costs and processes duration. Addressing these limitations, there is a call for a paradigm shift toward passivating the back contact.[18,19]

Theoretical considerations and simulations have indicated that a hole-selective-transport structure can enhance the efficiency of $Cu(In,Ga)Se_2$ solar cells, provided the selectivity of the hole-transport layer (HTL) is sufficiently high.[20–22] Various inorganic materials have been proposed for the HTL in chalcopyrite and other solar cells, including CuO_x,[23,24] $CuMO_x$ (M = Ga, In, Al, or Cr),[25–27] NiO_x,[28,29] and high bandgap $Cu(In,Ga)(S,Se)_2$.[30] In theory, these HTLs should be compatible with $Cu(In,Ga)Se_2$ solar cells. However, the main challenge lies in integrating the HTL within the back contact, as it needs to withstand the harsh conditions of the $Cu(In,Ga)Se_2$ deposition process: with a Se pressure of $\approx 10^{-6}$ Torr and temperatures exceeding 550 °C, all while maintaining good passivation and hole-transport properties. Most inorganic layer cannot withstand such conditions. For example, the Ni- and Cr-containing

T. Wang, S. Gharabeiki, M. Sood, A. C. M. Prot, R. G. Poeira,
M. Melchiorre, P. J. Dale, S. Siebentritt
Laboratory for Photovoltaics (LPV)
Department of Physics and Materials Science
University of Luxembourg
41 rue du Brill, L-4422 Belvaux, Luxembourg
E-mail: taowen.wang@uni.lu

L. Song, N. Valle, A.-M. Philippe, S. Glinsek, E. Defay
Materials Research and Technology Department (MRT)
Luxembourg Institute of Science and Technology (LIST)
rue du Brill 41, L-4422 Belvaux, Luxembourg

The ORCID identification number(s) for the author(s) of this article can be found under https://doi.org/10.1002/solr.202400212.

DOI: 10.1002/solr.202400212

materials are not suitable because they have been found to diffuse into the absorbers and form highly recombinative defects.[31] The key breakthrough of this study is the development of a novel, functional HTL that exhibits good hole-transport properties and passivation effects comparable to those achieved by Ga grading.

The focus of this work is narrow bandgap $CuInSe_2$ ($E_g^{EQE} = 1.01$ eV) without Ga, aiming at an optimal bottom cell in tandem applications.[32] We introduce a thermally evaporated 100 nm $CuGaSe_2$ layer covered by a 50 nm solution combustion synthesized (SCS) In_2O_3 capping layer as the HTL. A strong ion exchange between In and Ga is observed after the absorber deposition, but the oxide layer is found to prevent any Ga diffusing into the absorber, demonstrating the good thermal stability of the complete structure. The best reported narrow bandgap Cu(In,Ga)Se_2 device employing a single Ga backside gradient showed an effective minority lifetime of ≈100 ns, which further improves to ≈400 ns with rubidium fluoride (RbF) postdeposition treatment (PDT).[33] Here, we demonstrate a $CuInSe_2$ absorber with an HTL structure that exhibits a lifetime of 113 ns without PDT, showcasing favorable comparison to the device with Ga back gradient. By employing the passivating HTL, we observe an increase in quasi-Fermi level splitting (ΔE_F) from 450 to 530 meV. The devices exhibit a respectable fill factor (FF) above 71%, indicating good hole-transport properties. Therefore, we experimentally demonstrate the desired paradigm shift in Cu(In,Ga)Se_2 solar cells, achieving high efficiency without a Ga gradient and instead utilizing a passivating HTL, without sacrificing performance. Furthermore, simulations based on our experimental findings indicate that by optimizing the absorber, such as enhancing doping density, lifetime, and mitigating tail states, it is potential to achieve an efficiency of 22%.

2. Results and Discussion

2.1. Thermal Stability of the HTL

The as-grown HTL consists of a $CuGaSe_2$ layer, stabilized by a thin In_2O_3 layer. **Figure 1**a depicts the sample preparation procedure:[34] ≈100 nm $CuGaSe_2$ is co-evaporated onto Mo-covered glass substrates at setting temperature of 356 °C, followed by the deposition of 50 nm In_2O_3 using SCS at different annealing temperatures (200, 250, and 300 °C). The impact of In_2O_3 annealing temperature and its optimization process is discussed in Figure S1, Supporting Information. In brief, the higher annealing temperature of the In_2O_3 film removes impurities and leads to a longer lifetime and higher doping density in the absorber, thus 300 °C is selected as the optimized annealing temperature of In_2O_3. For the sample with extra NaF, 4 nm NaF is added on the top of the CGSe at substrate-setting temperature of 356 °C. The source temperature of NaF is 680 °C for the tip and 580 °C for the base, which gives us rough evaporation rate of 0.5 nm m^{-1}. A 1.8 μm $CuInSe_2$ layer is then grown by a three-stage process at substrate-setting temperature of 570 °C during stage 2 and 3.[35] When growing absorbers, the heating ramp is 50 °C m^{-1} and cooling ramp is 20 °C m^{-1}. To passivate the front surface and avoid surface degradation,[36,37] the samples are covered with a chemical bath deposited (CBD)–CdS layer for photoluminescence (PL) measurements and solar cell devices. Device fabrication involves sequential deposition of i-ZnO/ZnO:Al double-window layers and Ni/Al grids. Additional details are provided in Experimental Section.

The first critical issue to answer is the thermal stability of this novel HTL, which means this HTL should physically stay at the backside after the absorber growth. Scanning electron microscope (SEM) cross-section images in Figure 1b clearly show that the initial thickness of In_2O_3 and $CuGaSe_2$ before the $CuInSe_2$ deposition is around 50 and 100 nm, respectively. After the $CuInSe_2$ deposition, the individual stack of two layers can still be easily identified and their respective thicknesses remain unchanged, which indicates that the In_2O_3 is a good stabilizer that blocks the massive out-diffusion of Ga.

The SEM cross-section images show two distinct layers remaining at the backside, after the absorber deposition, indicating the good thermal stability of the HTL. To investigate further, transmission electron microscopy (TEM) analysis was conducted on the near backside interface. **Figure 2**a,b displays the TEM cross-section image, with Figure 2a showing the TEM image

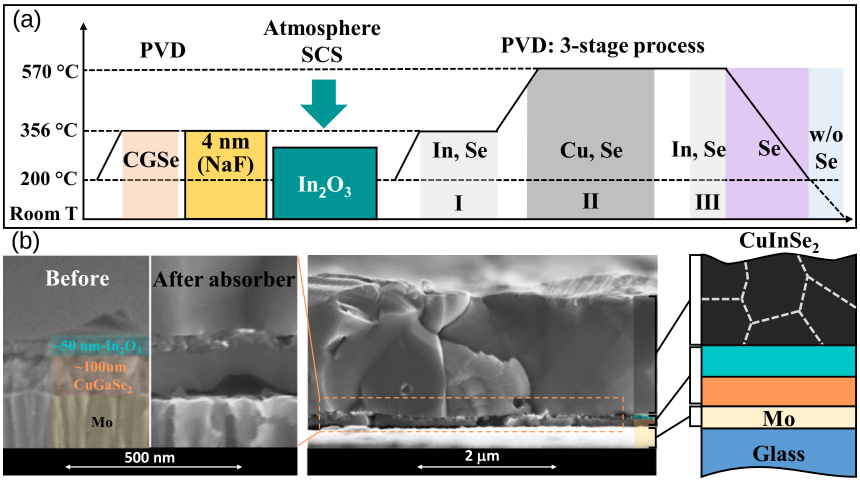

Figure 1. Sample preparation and stability of HTL. a) Procedure to prepare $CuInSe_2$ samples with hole-selective-transport layer; b) SEM cross-section images showing that the thickness of the two layers does not change after the $CuInSe_2$ deposition, which indicates the good thermal stability of the HTL.

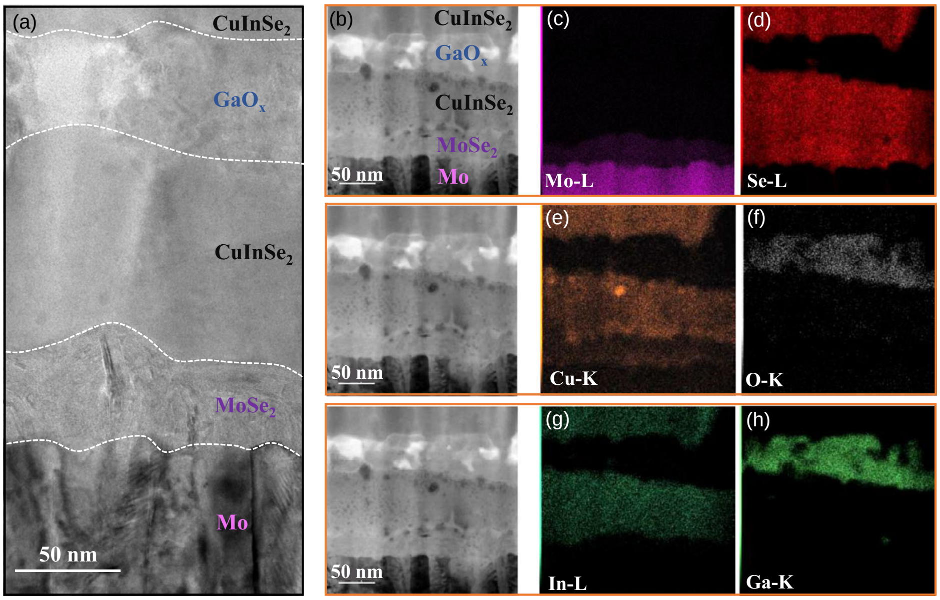

Figure 2. TEM measurements. a) TEM cross-section image from Mo (bottom) to $CuInSe_2$ (top); b) bright-field image STEM: cross-section image near the backside (three same images in vertical), with corresponding element mapping measured by EDS: c–h) the distribution of Mo, Se, Cu, O, In, and Ga, respectively.

and Figure 2b showing the bright-field scanning TEM (STEM) image. The corresponding elemental distributions are depicted in Figure 2c–h. The TEM image reveals a Mo layer at the bottom, while the layer above, likely $MoSe_2$, according to the elemental maps (Figure 2c,d) and in agreement with literature,[38–40] is less clear in Figure 2b but visible in Figure 2a. Additional evidence is provided in Figure S5, Supporting Information, showing a clear accumulation of Mo and Se in this region (at thickness ≈0.1 μm), suggesting the formation of $MoSe_2$. Above the $MoSe_2$ layer, there are two sequential layers corresponding to the layers shown in Figure 1b. The thickness of these layers is roughly the same as determined by the SEM cross-section image (Figure 1b), 50 nm of the capping layer and 100 nm of the under layer. The corresponding element mapping reveals a surprising result of complete ion exchange, forming a Ga oxide layer on top of a $CuInSe_2$ layer. The region rich in oxygen, represented by Figure 2f, indicates the location of the In_2O_3 before the absorber deposition. However, the presence of Ga instead of In suggests an extensive interdiffusion, as shown in Figure 2g,h. Conversely, the region containing $CuGaSe_2$ before the absorber deposition shows no detectable Ga but a significant In content. The element depth profile in Figure S5, Supporting Information, confirms that the oxide layer is Ga rich, while the layer beneath consists of Cu, In, and Se with minimal Ga. These findings indicate a strong In–Ga exchange during the absorber deposition, altering the $CuGaSe_2/In_2O_3$ combination prior to the absorber deposition to $CuInSe_2/GaO_x$.

The formation of $CuInSe_2/GaO_x$ was also confirmed through Raman and grazing-incidence X-ray diffraction (GIXRD) measurements performed on the backside of the sample (Figure S6, Supporting Information). The measured Raman peak at $174\,cm^{-1}$ (Figure S6b, Supporting Information) indicates the A_1 mode of Se–Se motion in $CuInSe_2$,[41] which is distinct from the A_1 mode of $CuGaGaSe_2$ with the peak at $183\,cm^{-1}$.[42] Additionally, GIXRD analysis (Figure S6c, Supporting Information) revealed a distinct orientation (112) of $CuInSe_2$ at 2θ of 26.7°. Moreover, the GIXRD data exhibited a broad diffraction peak around 2θ of 19.7°, which is highly indicative of β-GaO_x.[43] We would like to point out that, before the absorber process, X-ray diffraction (XRD) clearly indicates the existence of an In_2O_3 phase (Figure S1a, Supporting Information). Thus, the In–Ga ion exchange happens during the high-temperature absorber deposition. This exchange may be explained by the free energy differences of involved compounds. The following chemical reaction can be used to describe the process of exchange taking place between In and Ga:

$$2CuGaSe_2 + In_2O_3 \Leftrightarrow 2CuInSe_2 + Ga_2O_3 \tag{1}$$

According to the free energy values reported by Guillemoles,[44] the free energy difference of this reaction is around $-125\,kJ\,mol^{-1}$, which is a rather high driving force to promote the exchange of In and Ga. David Cahen et al.[45] reported a slightly lower free energy difference of $-91\,kJ\,mol^{-1}$, which is nevertheless enough to drive the exchange of In and Ga.

Despite the ion exchange between In and Ga, the oxide layer serves as an effective barrier to block Ga diffusion into the absorber. This is evident from Figure 2h (top region) and S5, Supporting Information (within a distance above 0.4 μm), where no Ga is detected in the absorber layer, indicating successful blocking by the oxide layer. As discussed earlier, achieving a homogeneous absorber is crucial to minimize non-absorption of long-wavelength photons. Therefore, the blocking effect of the oxide layer on Ga diffusion is crucial to avoid the formation of a Ga lateral profile. And it also proves that the passivation of backside recombination, discussed in the following, is due to the HTL rather than to any Ga gradient.

2.2. Passivation Effects of the HTL

We proceeded to investigate the passivation effects of the HTL, focusing on its ability to reduce backside recombination. Three samples have been considered: the reference sample without backside passivation, the HTL-passivated sample with In_2O_3 annealed at 300 °C, and the sample passivated with the same HTL as the second one but containing additional 4 nm NaF precursor. These samples are respectively labeled as "Mo-Re," "HTL-300," and "4 nm NaF" in **Figure 3**. The first indicator of effective passivation is the increase in effective lifetime of the $CuInSe_2$ absorber, as presented in Figure 3a. Since the absorbers and CdS coverage were prepared using the same recipe, it can be assumed that these samples have a similar bulk lifetime and front surface recombination velocity. Therefore, a longer effective lifetime measured by time-resolved photoluminescence (TRPL) signifies a lower backside recombination velocity and thus reduced backside recombination. Indeed, the slower PL transients in the HTL-passivated samples (Figure 3a) indicate a longer effective lifetime. The lifetimes, obtained from the weighted average of two-exponential fits to the PL transients, are presented in Figure 3b. For the sample with In_2O_3 annealed at 300 °C, the lifetime is improved from 5 to 73 ns. The passivation effect of this HTL is also demonstrated by its lower ΔE_F deficits or lower non-radiative losses when compared to the reference sample (estimated from $k_bT\ln[Y_{PL}]$, where Y_{PL} is the PL quantum yield (PLQY) that is determined by the absolute PL),[14,46,47] as shown in Figure 3b. However, the decrease in ΔE_F deficits is lower than the value predicated from its improvement in lifetime. Theoretically, assuming the same doping density, a one-order-of-magnitude longer lifetime corresponds to a ΔE_F gain of 59 meV,[47] represented by the dashed grey line in Figure 3b. The ΔE_F deficits of the HTL-passivated sample are above the grey line, suggesting that it may have lower doping density compared to the reference sample. To figure out the doping density of these samples, capacitance–voltage (C–V) measurements was used to determine the doping density. The apparent doping density depth profile obtained from C–V measurements is shown in Figure S4, Supporting Information. The doping density in Figure 3c is determined from the value at zero bias. In addition, the doping density is also estimated from the experimental ΔE_F and lifetime that are measured by PL-based techniques, absolute PL and TRPL, respectively. The PL method assumes flat quasi-Fermi levels throughout the absorber depth and determines the doping density based on the lifetime and ΔE_F, as discussed earlier.[11,48] The results from both methods confirm a lower doping density in the HTL-passivated samples. This reduction in doping density is likely due to the blocking of In_2O_3 not only of Ga but also of Na diffusion from the soda-lime glass. Therefore, to further enhance the ΔE_F, an additional 4 nm NaF layer is introduced between $CuGaSe_2$ and In_2O_3 (Figure 1a). This leads to an improved lifetime of 113 ns with a doping density only slightly lower than the reference sample, resulting in a ΔE_F of ≈530 meV (Figure 3d). The good passivation effect and doping density trend are further confirmed by the optical diode factor analysis. The details of the discussions are shown in Section S1, Supporting Information.

The passivation effect of the HTL is also demonstrated by the external quantum efficiency (EQE) spectra (Figure 5).

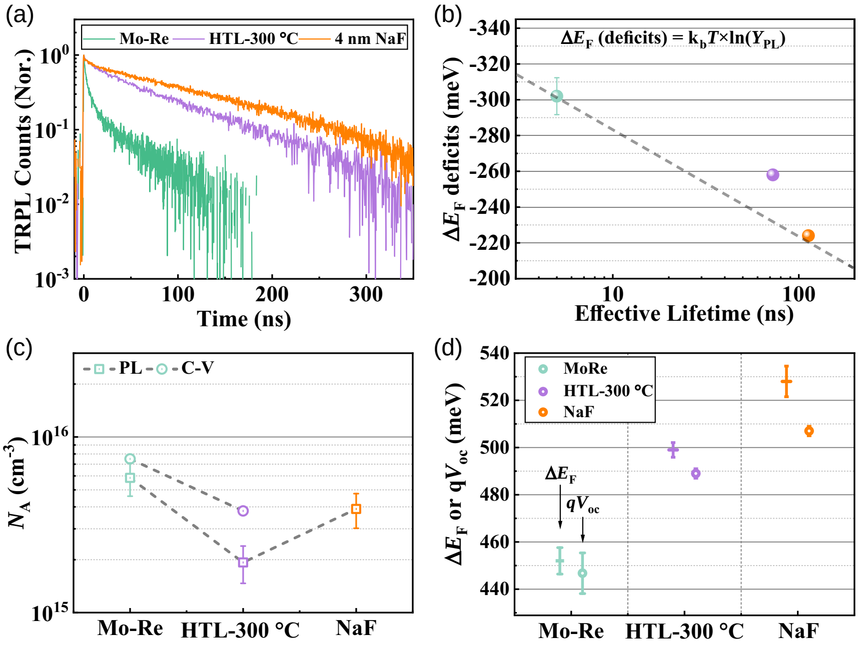

Figure 3. a) Time-resolved photoluminescence measurements. The extracted effective lifetimes of samples are shown in Figure 3b. The longer lifetime of samples with HTL, annealed at 300 °C, suggests a good passivation effect. Adding additional NaF precursor leads to a yet longer lifetime; b) the ΔE_F deficits due to non-radiative loss are determined by the PLQY. The improvement in ΔE_F of the HTL without additional Na is weaker than the expectation from the longer lifetime, due to lower doping density; c) the doping densities of samples are measured by C–V and as well as calculated from PL and TRPL. The lower doping density is likely due to the blocking of Na diffusion from the glass; d) the increase in V_{oc} follows the increase in ΔE_F.

We compare the EQE of the Mo reference sample, the HTL sample with NaF precursor, and a Ga single grading (GBG) sample from our previous work.[11] The steepest onset of absorption and collection is observed for the HTL sample. The reference sample with Mo back contact depicts a more gradual EQE edge because carriers generated near the back contact by long-wavelength irradiation have a lower chance to be collected due to the vicinity of the highly recombination active back contact. This loss is also reflected by an overall lower EQE. In contrast, the sample with backside gradient has lower absorption for long-wavelength irradiation: the low-bandgap region is considerably thinner than the whole-film thickness. A gradual onset of absorption can lead to additional radiative voltage losses.[13] Differences in the absolute value of EQE can mask the effect of the gradual absorption edge on the radiative loss. Therefore, to study the influence of the gradual absorption onset, we determine the radiative loss from the PL spectra, as defined in ref. [14], using the inflection point of the absorptance as the photovoltaic bandgap. We obtain 16.3 mV of the GBG sample, 16.6 mV of the $CuInSe_2$ reference sample on Mo back contact, and 15.2 mV of the HTL sample. The higher radiative loss of the reference sample is most likely due to an additional defect emission around 0.95 eV, which is only present in this sample. Thus, comparing the gradient sample and the HTL sample, the steeper absorption onset of the nongraded sample decreases the radiative loss by only 1 mV. The larger part of the radiative loss is due to tail states, as we discuss further later. The performance of devices serves as the final test for the new HTL. The V_{oc} aligns well with the improved ΔE_F as shown in Figure 3d, which validates the passivation effect. The sample with additional NaF exhibits a slightly higher deficit in ($\Delta E_F/q - V_{oc}$), most likely due to an increased front interface recombination.[49] Since we obviously reduce the backside recombination, this seems to demonstrate that the front interface with the buffer layer requires additional optimization.

The good passivation achieved by the HTL can be attributed to the conduction band offset between GaO_x and $CuInSe_2$, which has been shown in previous work.[50] Previous studies have reported the bandgap of GaO_x to be around 4.7 eV[51–55] and the electron affinity to be ≈3.2 eV,[53–55] although slight variations may exist depending on sample preparation and measurement methods. Nevertheless, these values do not significantly alter the conduction band offset between GaO_x and $CuInSe_2$, which is crucial for our discussion. By considering a bandgap of 4.7 eV and an electron affinity of 3.2 eV, we have plotted the potential band diagram of our solar cell in **Figure 4**, revealing a substantial conduction band spike. The presence of this high conduction band spike between GaO_x and $CuInSe_2$ effectively passivates the backside of the device by reducing the density of minority carriers at the metal surface, consequently minimizing backside recombination. To further illustrate the impact of the conduction band spike on backside recombination, we have conducted solar cell capacitance simulator (SCAPS) simulations. Further details and analysis can be found in Section S4, Supporting Information.

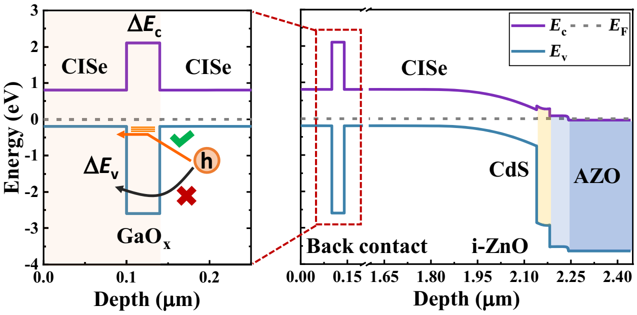

Figure 4. The proposed band structure of $CuInSe_2$ solar cell with $CuInSe_2/GaO_x$ as the HTL. The left figure is the magnification of the back contact part. The high conduction band minimum offset (ΔE_c) blocks the electrons reaching the metal surface, which reduces the electron density at the surface, and thus reduces the backside recombination. Theoretically, the high valance band offset (ΔE_v) is a hole-transport barrier that blocks the transport of holes. The surprisingly good hole-transport properties may be due to the Cu-related deep defects states. These states are close to the valence band maximum of the $CuInSe_2$ and assist the transport of holes.

2.3. Hole-Transport Properties of the HTL

A good HTL is more than just passivation, as it also requires good hole-transport properties to achieve a high FF.[20] In **Figure 5**a, the current density–voltage (J–V) characteristics do not show any hole-transport-blocking behavior (like rollover or S-shaped J–V curve), resulting in a good FF of over 71% (Figure 5b). This observation indicates that the developed HTL exhibits sufficient hole selectivity, enabling high $\Delta E_F(V_{oc})$ and FF simultaneously. However, the presence of GaO_x as a hole-transport-blocking layer is widely recognized, leading to limitation in diode current density and thus a low FF. The formation of GaO_x is a well-known issue during the high-temperature growth of $Cu(In,Ga)Se_2$ on transparent conductive oxide (TCO) contacts. At substrate temperatures above 450 °C, it is thermodynamically favorable for Ga to react with the TCO, resulting in the formation of GaO_x at the TCO and $Cu(In,Ga)Se_2$ interface.[56–58] GaO_x in these studies is typically amorphous with a high bandgap and resistance, forming a significant barrier for hole extraction. Consequently, the J–V curves exhibit an S shape or roll-over behavior due to the hole-transport-blocking caused by GaO_x.

We believe that the hole-transport ability of GaO_x is influenced by an excess Cu doping. Previous studies have reported that Cu can introduce deep acceptor states near the valence band maximum of $CuInSe_2$, as depicted in Figure 4. Density-functional theory calculations have predicted two Cu-related deep acceptor states,[59,60] which have also been observed through PL[61,62] and absorption measurements.[63] The defect transitions were found between 2.1 and 2.6 eV, which could be the defect close to the valence band of $CuInSe_2$. Thus, as depicted in Figure 4, it is plausible that Cu-related defect levels near the valence band maximum of $Cu(In,Ga)Se_2$ provide an additional hole-transport channel, facilitating hole transport. Similar defect-assisted carrier transport has been reported previously, where the transport of holes was facilitated by Cu-related defects in GaO_x[61] and $In_xGa_{2-x}O_3$[64] for perovskite solar cells. We could not detect Cu in the GaO_x layer by TEM X-ray energy-dispersive spectroscopy (TEM–EDS) (Figure 2e), but the detection limit is 1 at% and a Cu concentration lower than that might already generate enough defects to facilitate hole transport.

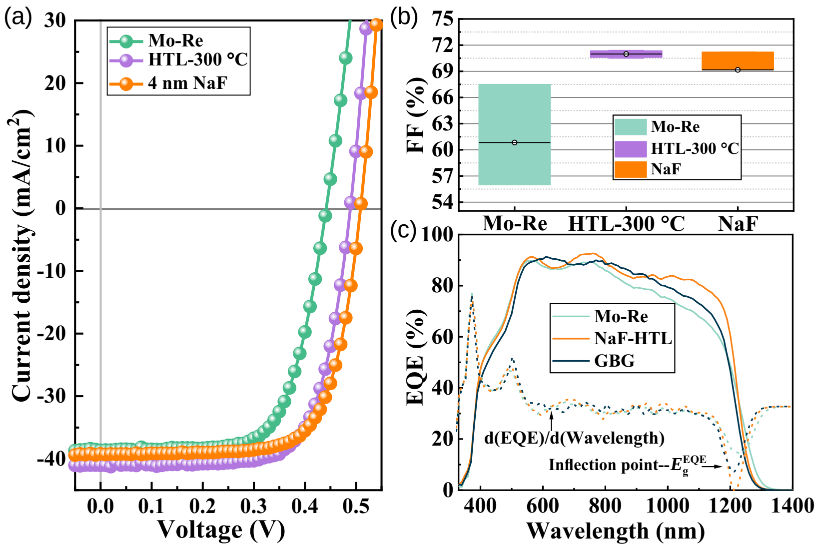

Figure 5. a) *J*–*V* curves show that there are no obvious carrier or current blocking barriers; b) fill factor of more than 71%, even higher than the reference sample, confirms good hole-transport properties. The number of solar cells is 4, 4, and 5 for the each series labeled as Mo–Re, HTL-300 °C and NaF, respectively; and c) the EQE of Mo reference sample, HTL-passivated sample with NaF precursor and GBG sample from our previous work.[11] The HTL sample has the best EQE response to long-wavelength photons, meaning the best collection of long-wavelength photon-generated carriers, thus the best backside passivation. The inflection point of the EQE shows the bandgap of the HTL-passivated sample is ≈1.01 eV.

In addition to In_2O_3, we also explored the implementation of GaO_x synthesized by SCS. However, the combination of $CuGaSe_2$ and GaO_x did not exhibit favorable passivation and hole-transport properties, as discussed in Section S6, Supporting Information. This suggests that the effective passivation and hole-transport properties of oxides may depend on factors such as morphology, composition (e.g., Ga/O ratio, Cu doping), and crystallization characteristics. The GaO_x in this case was amorphous, whereas the GaO_x formed by the ion exchange shows some crystallinity, as suggested by XRD in Figure S6c, Supporting Information.

2.4. Efficiency Loss Analysis

To discuss the efficiency loss of the solar cells with HTL, as shown in **Figure 6**a,b, we compare V_{oc} deficits and FF in relation to the effective lifetime between our devices and those obtained in state-of-the-art low-bandgap ($E_g^{EQE} \approx 1.01$ eV, obtained from the EQE inflection point) Cu(In,Ga)Se_2 devices with a GBG from AIST[65] and Empa.[32,33] The E_g^{EQE} of our HTL sample is the same as the samples from AIST and Empa as shown in Figure 5c. For the samples of AIST and Empa, the effective lifetime, measured by TRPL, and the doping density, determined by the *C*–*V* characterization, are taken from the respective publications. The dash lines in Figure 6a describe V_{oc} deficits with constant doping densities, obtained by assuming uniform carrier distribution, an absorber thickness of 2 μm, and no deficit between ΔE_F and V_{oc}. In reality, the V_{oc} is usually lower than the ΔE_F. To show this difference, 20 meV error of ΔE_F is allowed by the bands of the various doping densities, which shows a good agreement with the measured results. For example, the doping density of AIST sample and Empa sample after heavy alkali treatment, measured by *C*–*V*, is around 3×10^{16} and 2×10^{16} cm^{-3}, which agrees nicely with the estimated blue band. Our samples also show similar agreements. In terms of performances, our solar cell with the HTL structure has similar lifetime, FF, and V_{oc} deficits as the Empa device without heavy alkali (RbF) PDT. It can be expected that with an alkali treatment, our devices will also improve lifetime and doping density, thus reaching similar values as the state-of-the-art devices, however without the Ga back gradient. This supports the observation that the HTL structure developed in this work has similar passivation and transport properties as the optimized Ga grading. In other words, the paradigm shift has been performed.[18,19] Further improvement can be expected from the heavy alkali PDT, which roughly improves both doping density and lifetime by a factor of 4,[33] meaning a further improvement of V_{oc} of ≈70 mV.

A detailed analysis of V_{oc} losses of our device and their potential improvements are shown in Figure 6c. We start with the V_{oc}^{SQ} of a device with E_g^{EQE} of ≈1.01 eV: 776 meV (Shockley-Queisser model with a back reflector).[66] This voltage is reduced by the non-abrupt absorption edge, in particular by tail states. The V_{oc} loss of state-of-the art devices is determined only by tail states,[67] which includes both radiative and non-radiative losses. As discussed earlier, the larger part of the radiative loss in the solar cells discussed here is due to tail states. Non-radiative recombination via tail states also contributes to the V_{oc} loss,[67] as well as the joint effect of doping on tail states and V_{oc}.[68] We extract the Urbach energy E_u from PL spectra,[47] which is 12.9 meV for the best HTL sample (Figure S9, Supporting Information). For this Urbach energy, a V_{oc} loss of 150 mV would be expected, if it was only due to tail states.[67] However, the bulk V_{oc} loss, measured as the difference between ΔE_F and qV_{oc}^{SQ}, in the best device of this study is

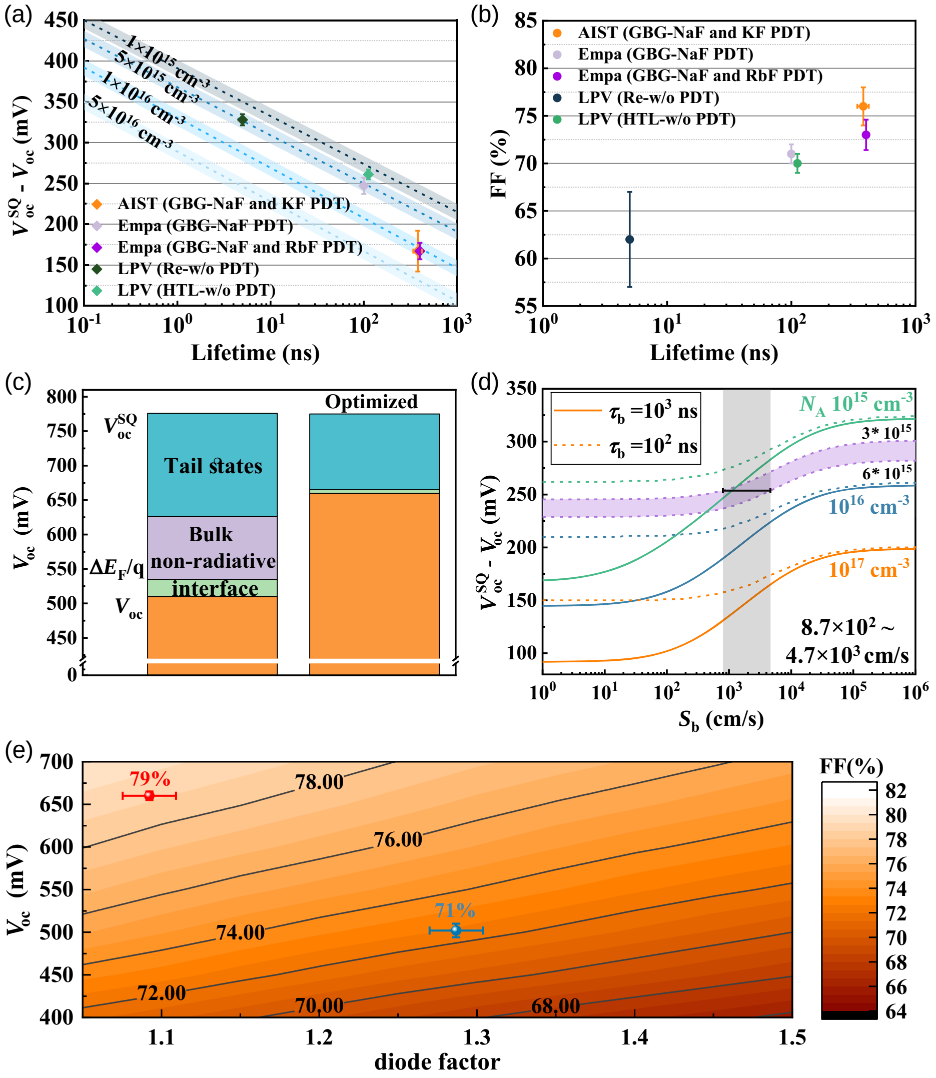

Figure 6. a,b) V_{oc} deficits ($V_{oc}^{SQ} - V_{oc}$) and FF of our reference (R_e) sample and the best sample (HTL) compared to the state-of-the-art low bandgap ($E_g = 1.01$ eV) Cu(In,Ga)Se_2 from AIST[65] and Empa;[32,33] c) V_{oc} losses analysis of the best sample and the potential losses that can be further minimized. The V_{oc} loss due to tail states includes both radiative and non-radiative recombination. Tail states broaden the absorptance [$A(E)$], which makes it away from step function like absorptance, thus increasing the radiative loss of V_{oc}. They can also cause non-radiative recombination via SRH recombination. The "Bulk non-radiative" loss of V_{oc} specifically means the loss due to low doping and SRH recombination assisted by deep defects or grain boundaries; d) SCAPS simulations of V_{oc} deficits as a function of back surface recombination velocity S_b with different lifetime and doping density; e) influence of V_{oc} and diode factor on FF by simulation of a one-diode model: the blue data point is our best sample with a diode factor ≈1.33, $V_{oc} = \approx 505$ mV and FF = ≈71%. With optimized V_{oc} and diode factor, the red data point suggests an achievable FF of ≈79% with a diode factor of 1.1 and $V_{oc} = 661$ mV.

241 meV, indicating additional non-radiative losses in the bulk due to low doping and Shockley-read-hall recombination (SRH) recombination assisted by deep defects or grain boundaries. In an optimized device, this loss becomes negligible.[67] As shown in the Figure 6c, the "bulk non-radiative" should be removed in an optimized case, then the V_{oc} loss of the solar cell will be dominated by tail states, i.e., the V_{oc} loss will be given by the Urbach energy and the empirical line in ref. [67]. We expect to get there by optimizing Na supply and heavy alkali PDT.

Additionally, the V_{oc} is lower than ΔE_F by 20 meV, demonstrating interface losses,[49] likely at the front interface. In state-of-the-art devices, this interface loss is as small as ≈5 mV.[69] Therefore, in our optimized device, we assume a 15 mV lower interface loss. For the very good Cu(In,Ga)Se_2 solar cells with an efficiency over 20%, the Urbach energy is around 11 meV,[67] reducing the tail states related losses to 110 mV. This takes us to an optimized V_{oc} of 661 mV. A similar improvement due to longer lifetime and higher doping density is demonstrated by SCAPS simulations[70] (Figure 6d). Sufficient doping and long lifetime are essential to gain higher V_{oc}, which is seriously reduced by back surface recombination. Depending on the PL method determined doping density and TRPL determined lifetime, within an error range, the back surface recombination velocity (S_b) of the best HTL sample is around 8.7×10^2 to

4.7×10^3 cm s^{-1}, which is estimated by comparing SCAPS-simulated V_{oc} losses to measured values, as in ref. [11]. With a bulk lifetime of 100 ns, a change of the back surface recombination velocity between 10^2 and 10^3 cm s^{-1} has a negligible impact on V_{oc}. However, with a lifetime of 1 μs, the back surface recombination velocity needs to be lower than $S_b < 10^2$ cm s^{-1} to make the V_{oc} loss independent of back surface recombination. At the same time, the effect of back side recombination is stronger for the lower doped case, because the low majority carrier concentration in combination with the long lifetime and low backside recombination, 1-sun illumination is already beyond low excitation, thereby reducing SRH recombination.

Regarding the FF, the FF of the best HTL sample is very similar to the Empa sample, without RbF PDT, with 71%. After the RbF PDT, the improvement in FF is around ≈2%. In addition to the Empa sample, the AIST solar cells with KF PDT show an even higher FF of 78%, which suggests that another ≈5% of FF can be gained by optimizing parasitic resistance (series resistance [R_s] and shunt resistance [R_{sh}]) as well as V_{oc} and diode factor. The R_s and R_{sh} of the best HTL sample are around 0.5 and 800 Ω cm^2, respectively, which are comparable to state-of-the-art values of the low-bandgap Cu(In,Ga)Se$_2$ solar cells. We would like to mention that our best samples with a Ga back gradient show an FF of 75%.[11] It is a challenge to further reduce R_s to 0.2 Ω cm^2 and increase R_{sh} to 2000 Ω cm^2, which can gain ≈3% of FF. The largest gain of FF is expected from reducing the diode factor and improving V_{oc}.[71] As we have shown previously,[72] the diode factor can be decreased by limiting the influence of metastable defects. We also present a simulation based on a two-diode model (actually it is a one-diode model, with the second diode being screened by using an extremely small J_{02}) that shows the influence of V_{oc} and diode factor on FF, as shown in Figure 6e. In this simulation, the R_s and R_{sh} is fixed to 0.5 and 1000 Ω cm^2, respectively. According to what we discussed previously, a V_{oc} of 661 mV appears realistic and a diode factor of 1.1 has been observed in sufficiently passivated and sufficiently doped Cu(In,Ga)Se$_2$ films.[71] Thus, we believe that the FF could be further increased from ≈71% to 79%, which potential leads to an efficiency of 22%. To achieve such a high efficiency, it is important to improve doping density, lifetime, and interface simultaneously.

3. Conclusion

We demonstrate the paradigm shift for chalcopyrite solar cells from Ga grading to HTL structure, which is a development that may open a new chapter for chalcogenide thin-film solar cells research and manufacturing. The CuGaSe$_2$ layer coated with an In$_2$O$_3$ stabilizer serves as an HTL. During the absorber deposition, a significant ion exchange between In and Ga takes place, leading to the transformation of CuGaSe$_2$/In$_2$O$_3$ into CuInSe$_2$/GaO$_x$. The good thermal stability, passivation, and hole-transport properties of developed HTL have been confirmed. Simultaneously, it has been observed that the oxide layer acts as a diffusion barrier, effectively confining all the Ga within the oxide layer and preventing the formation of a Ga gradient. By implementing the HTL structure, we successfully enhance the lifetime of CuInSe$_2$ samples from 5 to 113 ns, on par with state-of-the-art devices without heavy alkali treatment, accompanied by an increase in the ΔE_F of ≈80 meV, affirming the passivating effect of this novel HTL. Furthermore, the observed FF of over 71% in the device utilizing the HTL signifies good hole transport without current blocking effects. Considering the potential for further optimization, we anticipate achieving a solar cell efficiency of 22% for a pure CuInSe$_2$ absorber without Ga gradient. This can be accomplished by fine-tuning the sodium supply and implementing heavy alkali PDT, which will enhance both the doping density and lifetime of the absorber. With the results of this work, we have proved the possibility of making high-efficiency chalcopyrite solar cells without Ga gradient.

4. Experimental Section

Sample Preparation: **Mo:** The 500 nm molybdenum was prepared by sputtering.

CuGaSe$_2$: The 100 nm CuGaSe$_2$ was deposited by co-evaporation with a substrate temperature of 356 °C.

In$_2$O$_3$ and Ga$_2$O$_3$: The In$_2$O$_3$ was prepared by SCS. In$_2$O$_3$ combustion solution was prepared following the work reported by Kim et al.[73] In our case, the solution was prepared by dissolving 1203.2 mg of In(NO$_3$)$_3$·xH$_2$O (99.99%, Sigma Aldrich) in 20 mL of 2-methoxyethanol (2-MOE, 99.8%, Sigma-Aldrich) to form a 0.2 M solution. The 800 μL of acetylacetone (C$_5$H$_8$O$_2$, 99%, Sigma-Aldrich) was added as a fuel to the solution. An amount of 360 μL of 14.5 M NH$_3$ (aqueous, 99%, Sigma Aldrich) was added to raise the pH and promote the formation of In(acac)$_x$ (acac = C$_5$H$_7$O$_2$) complexes of In ions. The solutions were then stirred until they became clear. With this clear solution, the In$_2$O$_3$ films were prepared by spin-coating the solution at 3000 rpm for 60 s on the substrates, followed by hot-plate heating at 130 °C for 1 min. The process of spin-coating–drying was repeated four times to achieve 50 nm thickness. Finally, the crystallization of films was performed by placing the samples on a hot plate in air with the setting temperature varying from 200 to 350 °C for 3 min. The Ga$_2$O$_3$ was prepared by the same method and procedure, the only difference was replacing In(NO$_3$)$_3$·xH$_2$O (99.99%, Sigma-Aldrich) by Ga(NO$_3$)$_3$·xH$_2$O (99.99%, Sigma Aldrich).

CuInSe$_2$: The CuInSe$_2$ absorber was prepared with a typical three-stage process. At the first stage, the In–Se precursor was formed at a low-substrate-setting temperature of 356 °C. At the second stage, the Cu and Se were added to the film with a substrate-setting temperature of 570 °C. When it becomes slightly Cu rich (Cu/In ≈ 1.05 that is estimated from the growth process, e.g., from the first stoichiometric point), the Cu shutter was closed and the film was annealed in a Se atmosphere for 20 min. At the third stage with the same substrate-setting temperature of 570 °C, In and Se were supplied again to make the final absorber slightly Cu poor (Cu/In = 0.95 that is determined by EDS) with a thickness of ≈1.8 μm. The substrate temperature read from the pyrometer was usually lower than the setting temperature. The higher the setting temperature was, the larger the temperature difference. For the low temperature, e.g., 365 °C, they were more or less the same. For the high temperature, e.g., 570 °C, the temperature from the pyrometer was 50–60 °C lower than the setting temperature. In our PVD system, we maintained a minimum substrate temperature of 200 °C to prevent Se condensation on the substrate heater. Thus, as depicted in Figure 1a, the initial temperature for PVD processes was consistently set at 200 °C. Upon placement onto the substrate heater, samples underwent automatic heating to reach this temperature. Subsequently, during the cooling process, samples were gradually cooled down to around 200 °C within a Se atmosphere before being transferred to a buffer chamber. Here, they were naturally cooled down to the room temperature under a vacuum of ≈10^{-8} Torr. Throughout PVD operations, the heating ramp was set to 50 °C m^{-1}, while the cooling ramp was maintained at 20 °C m^{-1}.

CdS: The CdS was prepared by CBD. Before CdS covering, all samples were chemically etched with 5% aqueous KCN solution for 30 s to remove potential residual oxides. The CBD recipe was 6–7 min deposition at 67 °C with 2 mM $CdSO_4$, 50 mM thiourea, and 1.5 M NH_4OH. The estimated thickness was 40–50 nm according to typical growth rates. The CdS was necessary to passivate the front surface and prevent surface degradation.

TCO and Grids: To finish the devices, the i-ZnO/ZnO:Al were sputtered on the top of the CdS followed by e-beam-evaporated Ni/Al grids. The TCO deposition was performed in a commercial semiautomated sputtering deposition system. Two of the magnetron guns were equipped with ceramic 3 in diameter by 0.125 in thick ZnO and ZnO:Al (2 wt% of Al) targets powered by RF generators and operated in non-reactive Ar atmosphere. In the deposition of nonconductive ZnO (i-ZnO) and conductive ZnO:Al (AZO) films, the sputtering power applied to the target was fixed to 125 and 140 W, respectively, and the pressure was set at 1 mTorr. The thickness of the i-ZnO and AZO films was 80 and 380 nm, respectively.

Alkali Precursor: To improve Na doping, the 4 nm NaF precursor was added between $CuGaSe_2$ and In_2O_3 by thermal evaporation. The source-setting temperature was 580 °C for the base and 680 °C for the tip. The substrate-setting temperature was 356 °C.

Characterization: **TRPL:** This technology was based on time-correlated single-photon counting, which was used to measure luminescence decays in the time domain. Measurements were taken with a 640 nm pulsed diode laser. For samples with a short/long lifetime, the laser repetition rate was 5 MHz/2 MHz. The typical average power of the laser with repetition rate of 2 MHz was 0.25 mW. And the diameter of the laser was around 0.8 mm. To avoid the pileup effect that leads to the loss of long-lifetime photons, the ratio between total count rate and repetition rate is always kept below 2% by adjusting the waveguide iris filter to reduce the laser intensity if needed. A two-exponential decay function was used to fit the PL decay curve, and the weighted effective lifetime was considered:

$$\tau_e = \frac{A_1\tau_1 + A_2\tau_2}{A_1 + A_2} \tag{2}$$

where A_1 and A_2 are the prefactors for the τ_1 and the τ_2 decay, respectively. The details of fitting parameters are shown in Table S1, Supporting Information.

Absolute PL: The absolute PL was measured by a homebuilt setup. All samples were excited by a diode laser with a wavelength of 660 nm and measured in air at room temperature. The diameter of the laser was ≈2.6 mm. The photoluminescence was first collected by two parabolic mirrors and then redirected to a monochromator via a 550 μm optical fiber. The light was then detected by an InGaAs array detector. All PL spectra were spectrally corrected using a calibrated halogen lamp. Quantification of both excitation flux and spectrally corrected radiation flux was done by a powermeter, which allowed us to calculate ΔE_F with specific illumination intensities from 0.01 sun, even lower, to dozens of sun equivalents, depending on the quality and E_g of absorbers. The 1 sun intensity meant that the photon flux equaled to AM1.5 spectrum above the bandgap E_g of the absorber. According to Lambert–Beer's law and Planck's generalized law in Boltzmann approximation,[48] with the temperature fixed to the measured temperature of 296 K, the ΔE_F could be calculated by fitting the high-energy wing of the PL spectra where we assumed the absorptance equal to 1 ($A(E) = 1$). The ΔE_F might be slightly underestimated due to our assumption that $A(E) = 1$ for high-energy photons. We discussed recently the effect of $A(E) < 1$ for high-energy photons.[14]

With the ΔE_F, the $A(E)$ at low energies can be recalculated from the Planck's generalized law with the Boltzmann approximation:[48]

$$A(E) = \frac{\varnothing_{PL}(E)}{\varnothing_{bb}(E)\exp\left(\frac{\Delta E_F}{k_b T}\right)} \tag{3}$$

where $\phi_{PL}(E)$ is the measured PL spectrum, $\phi_{bb}(E)$ is the black body radiation, and k_bT is the thermal energy. Based on the Lambert–Beer's-law-neglecting reflection, the absorption coefficient [$\alpha(E)$] can be simplified as

$$\alpha(E) = -\frac{ln[1 - A(E)]}{d} \tag{4}$$

where the d is the thickness of the sample. The $\alpha(E)$ with respect to the photon energy could be plotted. By fitting the low energy part, the Urbach energy (E_U) of the sample could be determined according to the model:[74]

$$\alpha(E) = \alpha_0 \exp\left(-\frac{E_0 - E}{E_U}\right) \tag{5}$$

where the α_0 and E_0 are fit parameters. The so-called Urbach energy described the tail states exponentially extended from the band edges into the forbidden band, which gave an indication about how many tail states existed in the absorber. The larger Urbach energy suggested the more tail states that caused the higher radiative and non-radiative loss in ΔE_F.

C–V: The capacitance of the solar cell as a function of applied DC voltage was recorded using an inductance capacitance and resistance meter in the frequency range $f = 100$ Hz to 1 MHz with a controlled small-signal AC voltage amplitude of 30 mV rms. The *C–V* measurements were performed at low temperature with the frequency of 100 k Hz after keeping the device in dark at 300 K for 8 h to ensure a relaxed state. The low temperature was used to remove the capacitance contributed by the deep defects.

Illumination *J–V*: Measurements were carried out at 25 °C with a four-probe configuration. A class AAA solar simulator supplied a simulated AM1.5G spectrum that was calibrated by a Si reference cell. The forward scanning voltage was applied from −0.3 to 0.6 V with a step of 0.01 V. The area of the solar cells was measured by a calibrated microscope, which might give a small error of the J_{sc} that made it slightly different from the integrated J_{sc} from the EQE.

EQE: The EQE spectra were measured by a homebuilt setup, which contained a grating monochromator setup under a chopped illumination based on halogen and xenon lamps. And a lock-in amplifier was used to measure the photocurrent of the solar cell. The reference spectra which were used for calibration were determined by a standard Si detector (300–1100 nm) and a InGaAs detector (1100–1400 nm). The measured solar cells were connected using four pins and measured in two-probe configuration.

SEM: SEM was used to analyze the cross-sectional microstructures of the films.

TEM: For this study, cross-section TEM samples were prepared using a focused ion beam FEI Helios Nanolab 650. TEM was performed with a JEOL F200-Cold FEG. Elemental mapping and profiling were obtained by EDS in STEM mode. Count profile as displayed on Figure S5, Supporting Information, was obtained by averaging the elemental map signal over the height of the top image of Figure S5, Supporting Information.

XRD: GIXRD) patterns with an incidence angle a of 0.5° were recorded on a Bruker D8 Discover diffractometer (Bruker) using Cu-Kα radiation in the 2θ range from 20° to 60° with the step of 0.02°.

Raman: Raman spectroscopy was measured with a Renishaw inVia micro-Raman spectrometer equipped with a 532 nm excitation laser source and a 2400 lines mm^{-1} grating.

Differential Scanning Calorimeter: The thermal behavior of the combustion precursor was analyzed by differential scanning calorimeter (Mettler Toledo 3+). The samples were prepared by drying the solutions at 100 °C overnight in ambient atmosphere. Measurements were performed from 25 to 350 °C with a heating rate of 10 °C min^{-1} in the air atmosphere.

Simulation: **SCAPS:** The SCAPS could not directly simulate the influence of grain boundaries, but the overall influence of grain boundaries was modeled by the lifetime. The simulation baseline was based on the work of Gloeckler et al.[75] and the setting parameters can be found in **Table 1**.

"2-3 diode fit" Simulations (FF as a Function of V_{oc} and Diode Factor): The simulation was done by the "2-3 diode Fit" tool that was developed by Suckow et al.[76] This tool was based on a two-diode model; however, we kept the saturation current of the second diode (J_{02}) as small as 10^{-16} A cm^{-2}, which meant that the effect of the second diode was negligible, and thus it could be treated as a one-diode model. The R_s, R_{sh}, and J_{sc} used in simulation were fixed to 0.5 Ω cm^2, 1000 Ω cm^2, and 39.2 mA cm^{-2} that are from our experimental results. The different V_{oc}

Table 1. Parameters used in SCAPS simulation.

Parameters		AZO	i-ZnO	n-CdS	$CuInSe_2$	GaO_x
Thickness	d [µm]	0.2	0.06	0.05	2	0.04
Bandgap	E_g [eV]	3.3	3.3	2.4	1.02	4.7
Electron affinity	χ [eV]	4.6	4.6	4.4	4.5	3.2
Dielectric permittivity	ε (relative)	9	9	10	13.6	9
Effective density of states in the conduction band	N_c [cm^{-3}]	2.2×10^{18}				
Effective density of states in the valence band	N_v [cm^{-3}]	1.8×10^{19}				
Electron thermal velocity	e-V_{th} [$cm\ s^{-1}$]	10^7				
Hole thermal velocity	h-V_{th} [$cm\ s^{-1}$]	10^7				
Electron mobility	e-mobility [$cm^2\ V^{-1}s^{-1}$	100				
Hole mobility	h-mobility [$cm^2\ V^{-1}s^{-1}$]	25				
Shallow acceptor density	N_A [cm^{-3}]	–	–	–	10^{15}–10^{17}	–
Shallow donor density	N_D [cm^{-3}]	10^{20}	10^{18}	10^{17}	–	–
Effective radiative recombination coefficient	B [$cm^3\ s^{-1}$]	–	–	–	4.3×10^{-13}	–
Defect type		D	D	A	Neutral	Neutral
Electron capture cross section	σ_n [cm^2]	10^{-15}	10^{-15}	10^{-17}	10^{-15}	10^{-15}
Hole-capture cross section	σ_h [cm^2]	10^{-13}	10^{-13}	10^{-12}	10^{-15}	10^{-15}
Defects density (neutral)	N_t [cm^{-3}]	10^{17}	10^{17}	10^{18}	10^{14}–10^{15}	10^{17}
Defects position		0.1 eV below E_c		0.1 eV above E_v	Mid gap	
Defects distribution	E_t distribution	Uniform				
Surface condition						
Parameters		**Back surface**			**Front surface**	
Surface recombination velocity of electron	S_n [$cm\ s^{-1}$]	10^0–10^6			1.4×10^3 (ref. [7])	
Surface recombination velocity of hole	S_p [$cm\ s^{-1}$]	10^6			1.4×10^3	
Work function	W [eV]	Auto-flat band				

with specific diode factor was manipulated by adapting J_{01}, and then the corresponding FF was given.

Supporting Information

Supporting Information is available from the Wiley Online Library or from the author.

Acknowledgements

T.W. and L.S. contributed equally to this work. This work was supported by the Luxembourg National Research Fund (FNR) through the PACE project under the grant number of PRIDE17/12246511/PACE and MASSENA project under the grant number of PRIDE15/10935404 and TAILS project under the grant number of C20/MS/14735144/TAILS. The authors thank all developers of SCAPS at the Department of Electronics and Information Systems (ELIS) of the University of Gent. Dr. Vincent Roge at LIST is acknowledged for helping to perform SEM. Dr. Youri Nouchokgwe at LIST is acknowledged for helping to perform DSC. ChatGPT, a language model developed by OpenAI in San Francisco, CA, USA, provided assistance in English language editing. The whole text has been carefully modified and verified by the authors. For the purpose of open access, the author has applied a Creative Commons Attribution 4.0 International (CC BY 4.0) license to any author-accepted manuscript version arising from this submission.

Conflict of Interest

The authors declare that they have competing interests related to the patent associated with this work. The patent in question is (application no. LU504697) titled "Thin film solar cell and corresponding production method". The inventor Taowen Wang is an employee of University of Luxembourg. The inventor Longfei Song is an employee of Luxembourg Institute of Science and Technology (LIST). Both University of Luxembourg and LIST hold the patent and have a financial interest in the patent.

Data Availability Statement

The data that support the findings of this study are openly available in Zenodo at 10.5281/zenodo.10478799, reference number 10478799. The data can also be directly obtained from the corresponding author.

Keywords

backside passivations, chalcopyrites, Cu(In, Ga)Se_2 (CIGS), hole-transport layers (HTLs), thin-film solar cells

Received: March 13, 2024
Revised: May 3, 2024
Published online: May 27, 2024

[1] M. Powalla, S. Paetel, E. Ahlswede, R. Wuerz, C. D. Wessendorf, T. Magorian Friedlmeier, *Appl. Phys. Rev.* **2018**, *5*, 041602.
[2] T. Feurer, P. Reinhard, E. Avancini, B. Bissig, J. Löckinger, P. Fuchs, R. Carron, T. P. Weiss, J. Perrenoud, S. Stutterheim, *Prog. Photovolt: Res. Appl.* **2017**, *25*, 645.
[3] S. Siebentritt, T. Weiss, *Sci. China Phys. Mech. Astron.* **2023**, *66*, 217301.
[4] M. Nakamura, K. Yamaguchi, Y. Kimoto, Y. Yasaki, T. Kato, H. Sugimoto, *IEEE J. Photovolt.* **2019**, *9*, 1863.
[5] J. Keller, K. Kiselman, O. Donzel-Gargand, N. M. Martin, M. Babucci, O. Lundberg, E. Wallin, L. Stolt, M. Edoff, *Nat. Energy* **2024**, *9*, 467.
[6] P. Jackson, R. Wuerz, D. Hariskos, E. Lotter, W. Witte, M. Powalla, *Phys. Status Solidi –Rap. Res. Lett.* **2016**, *10*, 583.
[7] T. P. Weiss, B. Bissig, T. Feurer, R. Carron, S. Buecheler, A. N. Tiwari, *Sci. Rep.* **2019**, *9*, 1.
[8] P. Jackson, D. Hariskos, R. Wuerz, O. Kiowski, A. Bauer, T. M. Friedlmeier, M. Powalla, *Phys. Status Solidi –Rap. Res. Lett.* **2015**, *9*, 28.
[9] T. Dullweber, O. Lundberg, J. Malmström, M. Bodegård, L. Stolt, U. Rau, H.-W. Schock, J. H. Werner, *Thin Solid Films* **2001**, *387*, 11.
[10] A. M. Gabor, J. R. Tuttle, M. H. Bode, A. Franz, A. L. Tennant, M. A. Contreras, R. Noufi, D. G. Jensen, A. M. Hermann, *Sol. Energy Mater. Sol. Cells* **1996**, *41*, 247.
[11] T. Wang, F. Ehre, T. P. Weiss, B. Veith-Wolf, V. Titova, N. Valle, M. Melchiorre, O. Ramírez, J. Schmidt, S. Siebentritt, *Adv. Energy. Mater.* **2022**, *12*, 2202076.
[12] R. Carron, E. Avancini, T. Feurer, B. Bissig, P. A. Losio, R. Figi, C. Schreiner, M. Bürki, E. Bourgeois, Z. Remes, *STAM* **2018**, *19*, 396.
[13] U. Rau, B. Blank, T. C. Müller, T. Kirchartz, *Phys. Rev. Appl.* **2017**, *7*, 044016.
[14] S. Siebentritt, U. Rau, S. Gharabeiki, T. P. Weiss, A. Prot, T. Wang, D. Adeleye, M. Drahem, A. Singh, *Faraday Discuss.* **2022**, *239*, 112.
[15] Y. H. Chang, R. Carron, M. Ochoa, C. Bozal-Ginesta, A. N. Tiwari, J. R. Durrant, L. Steier, *Adv. Energy. Mater.* **2021**, *11*, 2003446.
[16] C. Spindler, F. Babbe, M. H. Wolter, F. Ehré, K. Santhosh, P. Hilgert, F. Werner, S. Siebentritt, *Phys. Rev. Mater.* **2019**, *3*, 090302.
[17] S. Siebentritt, A. Lomuscio, D. Adeleye, M. Sood, A. Dwivedi, *Phys. Status Solidi –Rap. Res. Lett.* **2022**, *16*, 2200126.
[18] B. J. Stanbery, D. Abou-Ras, A. Yamada, L. Mansfield, *J. Phys. D: Appl. Phys.* **2021**, *55*, 173001.
[19] M. Ochoa, S. Buecheler, A. N. Tiwari, R. Carron, *Energy Environ. Sci.* **2020**, *13*, 2047.
[20] U. Rau, T. Kirchartz, *Adv. Mater. Interfaces* **2019**, *6*, 1900252.
[21] A. Onno, C. Chen, P. Koswatta, M. Boccard, Z. C. Holman, *J. Appl. Phys.* **2019**, *126*, 183103.
[22] S. Sharbati, I. Gharibshahian, A. A. Orouji, *Opt. Mater.* **2018**, *75*, 216.
[23] M. R. Sultana, B. Islam, S. R. A. Ahmed, *Phys. Status Solidi A* **2022**, *219*, 2100512.
[24] I. Gharibshahian, A. A. Orouji, S. Sharbati, *Mater. Today Commun.* **2022**, *33*, 104220.
[25] F. Igbari, M. Li, Y. Hu, Z.-K. Wang, L.-S. Liao, *J. Mater. Chem. A* **2016**, *4*, 1326.
[26] J. Wang, T. B. Daunis, L. Cheng, B. Zhang, J. Kim, J. W. Hsu, *ACS Appl. Mater. Interfaces* **2018**, *10*, 3732.
[27] H. Zhang, H. Wang, W. Chen, A. K. Y. Jen, *Adv. Mater.* **2017**, *29*, 1604984.
[28] D. Xiao, X. Li, D. Wang, Q. Li, K. Shen, D. Wang, *Sol. Energy Mater. Sol. Cells* **2017**, *169*, 61.
[29] L. Xu, X. Chen, J. Jin, W. Liu, B. Dong, X. Bai, H. Song, P. Reiss, *Nano Energy* **2019**, *63*, 103860.
[30] L. Xu, L.-L. Deng, J. Cao, X. Wang, W.-Y. Chen, Z. Jiang, *Nanoscale Res. Lett.* **2017**, *12*, 1.
[31] F. Pianezzi, S. Nishiwaki, L. Kranz, C. M. Sutter-Fella, P. Reinhard, B. Bissig, H. Hagendorfer, S. Buecheler, A. N. Tiwari, *Prog. Photovolt: Res. Appl.* **2015**, *23*, 892.
[32] T. Feurer, R. Carron, G. Torres Sevilla, F. Fu, S. Pisoni, Y. E. Romanyuk, S. Buecheler, A. N. Tiwari, *Adv. Energy. Mater.* **2019**, *9*, 1901428.
[33] T. Feurer, F. Fu, T. P. Weiss, E. Avancini, J. Löckinger, S. Buecheler, A. N. Tiwari, *Thin Solid Films* **2019**, *670*, 34.
[34] T. Wang, L. Song, LU504697, Luxembourg Patent, **2023**.
[35] A. M. Gabor, J. R. Tuttle, D. S. Albin, M. A. Contreras, R. Noufi, A. M. Hermann, *Appl. Phys. Lett.* **1994**, *65*, 198.
[36] D. Regesch, L. Gütay, J. K. Larsen, V. Deprédurand, D. Tanaka, Y. Aida, S. Siebentritt, *Appl. Phys. Lett.* **2012**, *101*, 112108.
[37] F. Babbe, L. Choubrac, S. Siebentritt, *Appl. Phys. Lett.* **2016**, *109*, 082105.
[38] T. Wada, N. Kohara, S. Nishiwaki, T. Negami, *Thin Solid Films* **2001**, *387*, 118.
[39] S.-T. Kim, V. Bhatt, Y.-C. Kim, H.-J. Jeong, J.-H. Yun, J.-H. Jang, *J. Alloys Compds.* **2022**, *899*, 163301.
[40] Y.-I. Kim, K.-B. Kim, M. Kim, *J. Mater. Sci. Technol.* **2020**, *51*, 193.
[41] J. Álvarez-García, B. Barcones, A. Pérez-Rodríguez, A. Romano-Rodríguez, J. Morante, A. Janotti, S.-H. Wei, R. Scheer, *Phys. Rev. B* **2005**, *71*, 054303.
[42] C. Rincon, F. Ramirez, *J. Appl. Phys.* **1992**, *72*, 4321.
[43] S. Nakagomi, Y. Kokubun, *J. Cryst. Growth* **2012**, *349*, 12.
[44] J. Guillemoles, *Thin Solid Films* **2000**, *361*, 338.
[45] D. Cahen, R. Noufi, *J. Phys. Chem. Solids* **1992**, *53*, 991.
[46] L. Krückemeier, U. Rau, M. Stolterfoht, T. Kirchartz, *Adv. Energy. Mater.* **2020**, *10*, 1902573.
[47] S. Siebentritt, T. P. Weiss, M. Sood, M. H. Wolter, A. Lomuscio, O. Ramirez, *J. Phys.: Mater.* **2021**, *4*, 042010.
[48] P. Würfel, *Physics of Solar Cells*, Wiley-VCH Verlag GmbH, Weinheim **2005**.
[49] M. Sood, A. Urbaniak, C. Kameni Boumenou, T. P. Weiss, H. Elanzeery, F. Babbe, F. Werner, M. Melchiorre, S. Siebentritt, *Prog. Photovolt.: Res. Appl.* **2022**, *30*, 263.
[50] Y. Liu, Y. Sun, W. Liu, J. Yao, *PCCP* **2014**, *16*, 15400.
[51] M. Heinemann, J. Berry, G. Teeter, T. Unold, D. Ginley, *Appl. Phys. Lett.* **2016**, *108*, 022107.
[52] A. K. Mondal, R. Deivasigamani, L. K. Ping, M. A. Shazni Mohammad Haniff, B. T. Goh, R. H. Horng, M. A. Mohamed, *ACS Omega* **2022**, *7*, 41236.
[53] K. Kikuchi, S. Imura, K. Miyakawa, H. Ohtake, M. Kubota, *J. Phys.: Conf. Ser.* **2015**, *619*, 012008.
[54] H. Xue, Q. He, G. Jian, S. Long, T. Pang, M. Liu, *Nanoscale Res. Lett.* **2018**, *13*, 1.
[55] K. Kikuchi, S. Imura, K. Miyakawa, M. Kubota, E. Ohta, *Thin Solid Films* **2014**, *550*, 635.
[56] Y.-S. Son, H. Yu, J.-K. Park, W. M. Kim, S.-Y. Ahn, W. Choi, D. Kim, J.-H. Jeong, *J. Phys. Chem. C* **2019**, *123*, 1635.
[57] T. Nakada, *Thin Solid Films* **2005**, *480*, 419.
[58] S.-C. Yang, T.-Y. Lin, M. Ochoa, H. Lai, R. Kothandaraman, F. Fu, A. N. Tiwari, R. Carron, *Nat. Energy* **2023**, *8*, 40.
[59] H. Yan, Y. Guo, Q. Song, Y. Chen, *Phys. B* **2014**, *434*, 181.
[60] C. Zhang, Z. Li, W. Wang, *Materials* **2021**, *14*, 5161.
[61] J. Zhang, S. Zhu, C. Gao, C. Gao, X. Liu, *Sol. RRL* **2022**, *6*, 2100861.
[62] Y. Zhang, J. Yan, Q. Li, C. Qu, L. Zhang, W. Xie, *Mater. Sci. Eng. B* **2011**, *176*, 846.
[63] T. Gustafson, N. Giles, B. Holloway, C. Lenyk, J. Jesenovec, J. McCloy, M. McCluskey, L. Halliburton, *J. Appl. Phys.* **2022**, *131*, 065702.
[64] J. Zhang, S. Zhu, Q. Yang, C. Gao, X. Liu, *Sol. RRL.* **2017**, *1*, 1770114

[65] Y. Kamikawa, J. Nishinaga, H. Shibata, S. Ishizuka, *ACS Appl. Mater. Interfaces* **2020**, *12*, 45485.
[66] S. Rühle, *Sol. Energy* **2016**, *130*, 139.
[67] M. H. Wolter, R. Carron, E. Avancini, B. Bissig, T. P. Weiss, S. Nishiwaki, T. Feurer, S. Buecheler, P. Jackson, W. Witte, *Prog. Photovolt: Res. Appl.* **2022**, *30*, 702.
[68] O. Ramírez, J. Nishinaga, F. Dingwell, T. Wang, A. Prot, M. H. Wolter, V. Ranjan, S. Siebentritt, *Sol. RRL* **2023**, *7*, 2300054.
[69] M. H. Wolter, B. Bissig, E. Avancini, R. Carron, S. Buecheler, P. Jackson, S. Siebentritt, *IEEE J. Photovolt.* **2018**, *8*, 1320.
[70] M. Burgelman, P. Nollet, S. Degrave, *Thin Solid Films* **2000**, *361*, 527.
[71] T. P. Weiss, O. Ramírez, S. Paetel, W. Witte, J. Nishinaga, T. Feurer, S. Siebentritt, *Phys. Rev. Appl.* **2023**, *19*, 024052.
[72] T. P. Weiss, F. Ehre, V. Serrano-Escalante, T. Wang, S. Siebentritt, *Sol. RRL* **2021**, *5*, 2100063.
[73] M.-G. Kim, M. G. Kanatzidis, A. Facchetti, T. J. Marks, *Nat. Mater.* **2011**, *10*, 382.
[74] G. Cody, T. Tiedje, B. Abeles, B. Brooks, Y. Goldstein, *Phys. Rev. Lett.* **1981**, *47*, 1480.
[75] M. Gloeckler, A. Fahrenbruch, J. Sites, *presented at 3rd World Conf. on Photovoltaic Energy Conversion, 2003. Proc., Osaka*, **2003** (accessed: May, 2003).
[76] S. Suckow, T. M. Pletzer, H. Kurz, *Prog. Photovolt: Res. Appl.* **2014**, *22*, 494.